Available online at www.sciencedirect.com

ScienceDirect

Progress in Natural Science: Materials International 24 (2014) 184–190

Progress in Natural Science Materials International

www.elsevier.com/locate/pnsmi
www.sciencedirect.com

Original Research

Promotive effect of multi-walled carbon nanotubes on Co_3O_4 nanosheets and their application in lithium-ion battery

Yan Liu[a,*], Xiaogang Zhang[b], Chengkang Chang[a], Dongyun Zhang[a], Ying Wu[a,*]

[a]School of Materials Science and Engineering, Shanghai Institute of Technology, Shanghai 200235, China
[b]College of Material Science and Engineering, Nanjing University of Aeronautics and Astronautics, Nanjing, Jiangsu 210016, China

Received 7 November 2013; accepted 15 January 2014
Available online 22 May 2014

Abstract

Co_3O_4/MWCNTs composites have been synthesized by a simple hydrothermal method using a surfactant (CTAB) and a precipitation agent (urea). The samples were characterized by XRD, SEM and BET methods. The electrochemical properties of the samples as anode materials for lithium batteries were studied by EIS and Galvanostatic measurements. The Co_3O_4/MWCNTs composites displayed higher capacity and better cycle performance in comparison with the Co_3O_4 nanosheets. The remarkable improvement of electrochemical performance within the hybrid composites is probably related to the addition of MWCNTs that possesses improved properties such as excellent electric conductivity and large surface area, which helps to alleviate the effect of volume change, shorten the distance of lithium ion diffusion, facilitate the transmission of electron and keep the structure stable.

Keywords: Co_3O_4 nanosheets; Multi-walled carbon nanotubes; Hydrothermal method; Anode material; Lithium-ion batteries

1. Introduction

Nano-sized 3d transition metal oxides (Co, Ni, Fe or Cu) have extensively been investigated for new mechanisms and their potential applications in lithium ion batteries as anode materials. These transition metal oxide electrode materials exhibited excellent cycle reversibility and high specific capacity [1–6]. Among them, as an important magnetic p-type semiconductor, Co_3O_4 is of special interest due to its potential applications. However, Co_3O_4 often exhibits poor kinetics and severe capacity fading upon cycling mainly because of the low conductivity and the severe pulverization arising from the large volume change. Poor electronic conductivity of cobalt oxides limits them from application in high-performance lithium ion batteries. One of the other challenging issues is to tackle their capacity decay with cycling, occuring from large volume expansion during the lithium uptake/release process.

To overcome the above-mentioned problems, several strategies have been proposed to improve the cycle performance of transition-metal oxides by decreasing the particle size [7], using the metal oxide films or alloys [8], or dispersing metal oxides into an inactive/active matrix [9,10]. One of the most promising strategies is to disperse nanosized cobalt oxides into a carbon matrix, where carbon acts as both a structural buffer and an electrochemically active material during the lithium insertion/extraction [11–13].

Multi-walled carbon nanotubes (MWCNTs) have extraordinary mechanical, chemical and electrical properties. MWCNTs, due to their outstanding electrical properties apart from their high chemical stability, high aspect ratio, strong mechanical strength, and high activated surface area, are attractive electrode materials in energy storage devices, such as electrochemical capacitors, fuel cells, and lithium batteries [14–17]. Highly conducting MWCNTs enhance lithium storage

*Corresponding authors. Tel./fax: +86 21 60873439.
E-mail addresses: lyan@sit.edu.cn (Y. Liu), science2008@live.cn (Y. Wu).

Peer review under responsibility of Chinese Materials Research Society.

ELSEVIER Production and hosting by Elsevier

http://dx.doi.org/10.1016/j.pnsc.2014.05.001
1002-0071/

properties and the tubular morphology offers a unique combination of high porosity and low internal resistance, and meanwhile, MWCNTs also can buffer the volume changes of active particles and thus alleviate their pulverization [18–20]. Both of the two aspects are beneficial for the electrochemical properties of the cobalt oxides.

In the present work, Co_3O_4 nanosheets and Co_3O_4/MWCNTs composites as high-performance electrodes were prepared. An attempt had been made to synthesize Co_3O_4 nanosheets by using a surfactant (CTAB) and a precipitator (urea), and the electrochemical properties were studied to evaluate their applications in lithium ion battery.

2. Experimental

All the chemicals were of analytical purity and used as received. In a typical procedure, cobalt nitrate ($Co(NO_3)_2 \cdot 6H_2O$), cetyltrimethylammonium bromide (CTAB) and urea ($Co(NH_2)_2$) were added to 60 ml of distilled water with stirring. The mole ratio of $Co(NO_3)_2$: CTAB: Co $(NH_2)_2$ was 1:2:3. After stirring for 30 min, the solution was kept at 120 °C for 18 h in a Teflon-lined stainless steel autoclave for reaction. The precipitate was collected by centrifugation and washed with distilled water and absolute ethanol and finally heated at 300 °C for 3 h to obtain the desired product, which is named Sample 1.

MWCNTs were purchased from Shenzhen Nanotech Port Co. Ltd. (Shenzhen, China). MWCNTs were pretreated in concentrated nitric acid at 100 °C for 48 h, and then washed with de-ionized water and dried in vacuum at 60 °C for 8 h. Additionally, the acid treated MWCNTs were used as raw material and dispersed in the above solution by ultrasonication for 0.5 h and stirred for another 0.5 h. Thus, Sample 2 was obtained as mentioned above with MWCNTs added.

The phase purity of the product was characterized by X-ray power diffraction (XRD, Bruker D8 advance, Germany) with Cu Kα radiation (λ=0.1518 nm), employing a scanning rate of $10^\circ\ min^{-1}$ in the 2θ range from 10° to 70°. The scanning electron microscopy (SEM) images were obtained using a Leo 1430 VP microscope. Nitrogen adsorption–desorption isotherms were measured with a Micromeritics ASAP 2010 instrument at −196 °C. Samples were outgassed for 10 h under vacuum at 200 °C before measurement. The BET method was used to calculate the surface areas. The pore size distributions were derived from the adsorption branches of the Barrett–Joyner–Halenda (BJH) method.

The electrochemical properties of the powders were examined using a two-electrode electrochemical cell. The working electrodes were prepared by a slurry coating procedure. The slurry consisted of 80 wt% active material, 15 wt% acetylene black and 5 wt% polyvinylidene fluoride (PVDF) dissolved in N-methyl pyrrolidinone (NMP), and was spread on a nickel mesh current collector (diameter=11 mm). The mesh was dried in a vacuum oven for 12 h at 100 °C. Test cells were assembled in an argon-filled glove box using Li foil as a counter electrode and polypropylene (PP) film as separator. The electrolyte was 1M $LiPF_6$ in a 50:50 (w/w) mixture of ethylene carbonate (EC) and diethyl carbonate (DEC). The electrochemical impedance spectroscopy (EIS) of the electrode was performed on a SI 1260 electrochemical workstation (Solartron Analytical Inc.). The frequency of EIS ranged from 0.01 to 100 kHz at the open-circuit potential. A small ac signal of 5 mV in amplitude was used as the perturbation of the system throughout the tests. Charge–discharge cycles of the half-cells were measured between 0.01 and 3.0 V *vs.* Li/Li^+ at various current densities of 20, 40 and 60 mA g^{-1} using a Land CT 2001 A battery program-control test system. Current densities and specific capacities were calculated based on the mass of the active material. All electrochemical measurements were carried out at room temperature.

3. Results and discussion

Fig. 1 shows the XRD patterns of the calcined samples at 300 °C and no obvious peaks of impurities are detected. As shown in Fig. 1(a), the patterns have main diffraction peaks at 36.88°, 65.18°, 31.34°, 59.3° and 44.82° ((311), (440), (220), (511) and (400) reflections, respectively). All the diffraction peaks can be indexed to the typical Co_3O_4 phase (space group *Fd3m* [227]), which are consistent with the standard crystallographic data (JCPDS card no. 76-1802). Unlike the pure Co_3O_4, one diffraction peak at 25.8° is detected in Fig. 1(b), which corresponds to the diffraction peak of (002) of MWCNTs (JCPDS card no. 26-1079).

The SEM images of the samples are presented in Fig. 2. The pure Co_3O_4 powder presented a more uniform laminate structure as shown in Fig. 2(a) and (b). As for the MWCNTs-containing composites in Fig. 2(c) and (d), Co_3O_4 nanoparticles were an assembly of nanosheets. The size and morphology of the samples were changed by adding MWCNTs. The size of Sample 2 is smaller than those of Sample 1. MWCNTs disappeared among Co_3O_4 nanosheets. Regarding the mechanism for the growth of the Co_3O_4 powder, it is believed that urea provided a controlled and continuous source of OH^-. Urea is an alkaline substance; it is a non-toxic, stable, and nonionic, water-soluble compound. In the hydrothermal

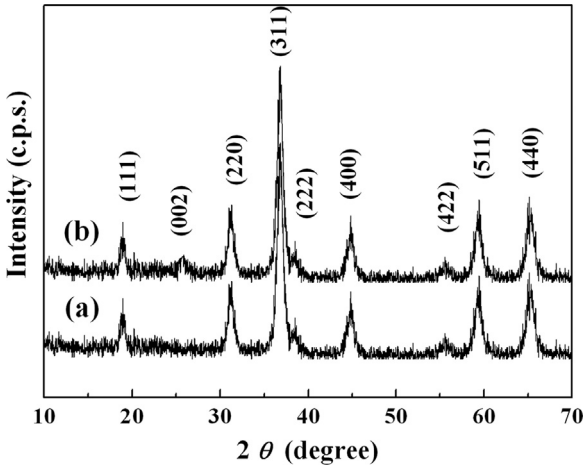

Fig. 1. XRD patterns of the calcined materials: (a) Sample 1 and (b) Sample 2.

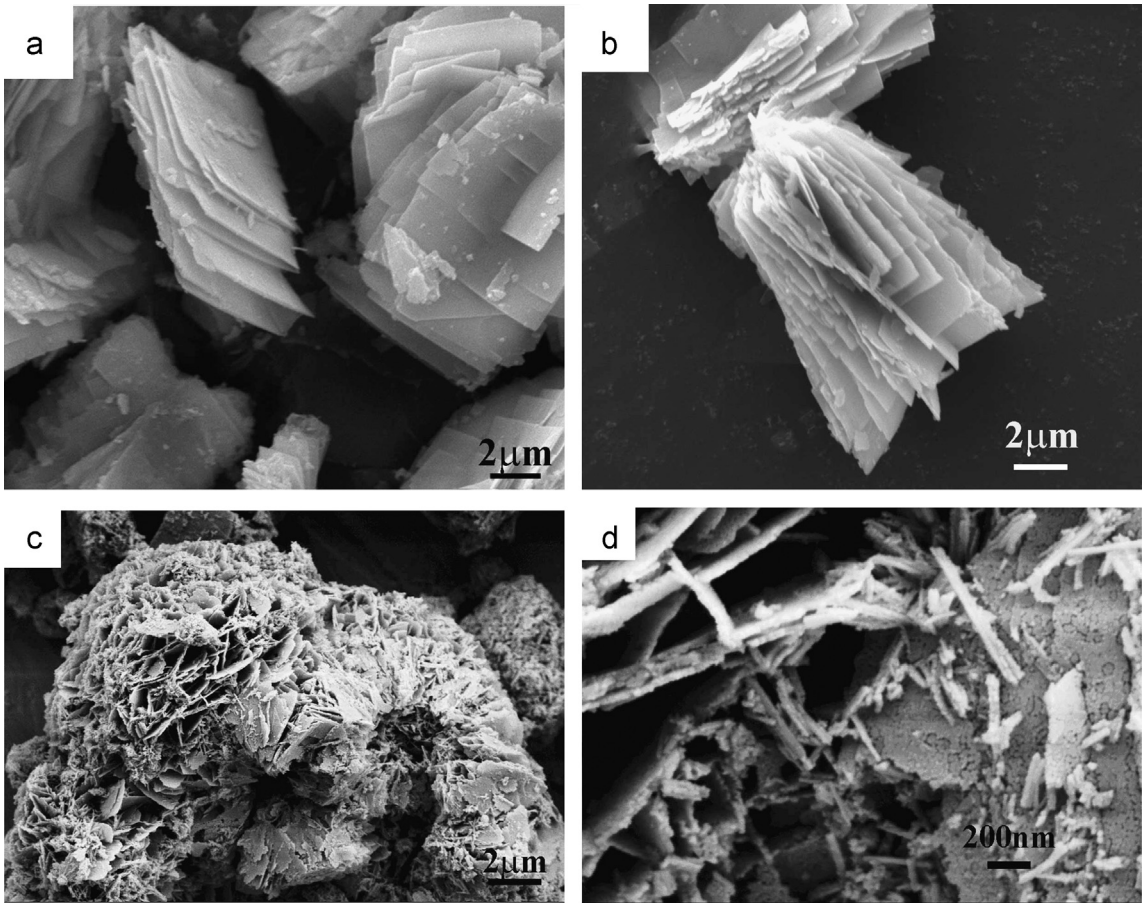

Fig. 2. SEM images of the calcined materials: (a, b) Sample 1 and (c, d) Sample 2.

reaction, the formation of tiny crystalline nuclei in a supersaturated medium firstly occurred and was then followed by crystal growth, which was based on the formation of a solid phase from the solution. In fact, urea could hydrolyze as the following equations in water solution.

$$H_2NCONH_2 + H_2O \rightarrow 2NH_3 + CO_2 \quad (1)$$

$$CO_2 + H_2O \rightarrow {CO_3}^{2-} + 2H^+ \quad (2)$$

$$NH_3 + H_2O \rightarrow {NH_4}^+ + OH^- \quad (3)$$

$$2{Co}^{2+} + 2OH^- + {CO_3}^{2-} \rightarrow Co_2(OH)_2CO_3 \quad (4)$$

$$3Co_2(OH)_2CO_3 + O_2 \rightarrow OCo_3O_4 + 3H_2O\uparrow + 3CO_2\uparrow \quad (5)$$

In the present experiment, CTAB is widely used as a surface active agent to adsorb on the surface of metal ions and to exert either hydrophobic or coulombic effects on metal ions, thereby as the template to form laminate structure and to stabilize them. Furthermore, the growth of the Co_3O_4 particles was suppressed by adding MWCNTs.

Fig. 3 shows the representative BJH pore size distributions and nitrogen gas adsorption–desorption isotherm plots of the samples. The isotherms are of type IV of the IUPAC classification. It is noticeable in Fig. 3(A) that Sample 1 has a broader distribution. A large hysteresis loop varying from P/P_0 0.55 to 0.88 and a small loop varying from about P/P_0 0.88 to 1 are observed. Furthermore, the pore size distributions in Fig. 3(B) are consistent with the nitrogen adsorption/desorption isotherm, which generally exhibits a bimodal size distribution with mean diameters of 2 and 10 nm. By comparison with Sample 1, Sample 2 has a narrower distribution, while the hysteresis loop moved right varying from P/P_0 0.6 to 1. The BET specific surface areas of Sample 1 and Sample 2 calculated from N_2 adsorption are 79.15 and 84.51 $m^2\,g^{-1}$, respectively. Thus, Sample 2 showed higher surface area.

Fig. 4 depicts the potential *vs.* capacity behaviors of Sample 1 and Sample 2 in the 1st, 5, 10, 15, 20, 25 and 30th galvanostatic discharge–recharge curves. Cycling took place between 0.01–3.0 V *vs.* Li/Li^+ at different cycling rates of 20, 40 and 60 mA g^{-1}. The corresponding charge–discharge capacities are presented in Table 1. From Table 1, the capacity loss (CL) of Sample 1 (798.4 mAh g^{-1}) was larger than that of Sample 2 (478.8 mAh g^{-1}) in the first discharge–charge curve. The irreversible capacity during the first cycle was reduced by adding MWCNTs. It also can be seen that the potential plateaus of Sample 2 got lower than those of Sample 1 during the charge–discharge progress. It is noted from Fig. 4 that the charge (Li extraction) capacities decreased by increasing the

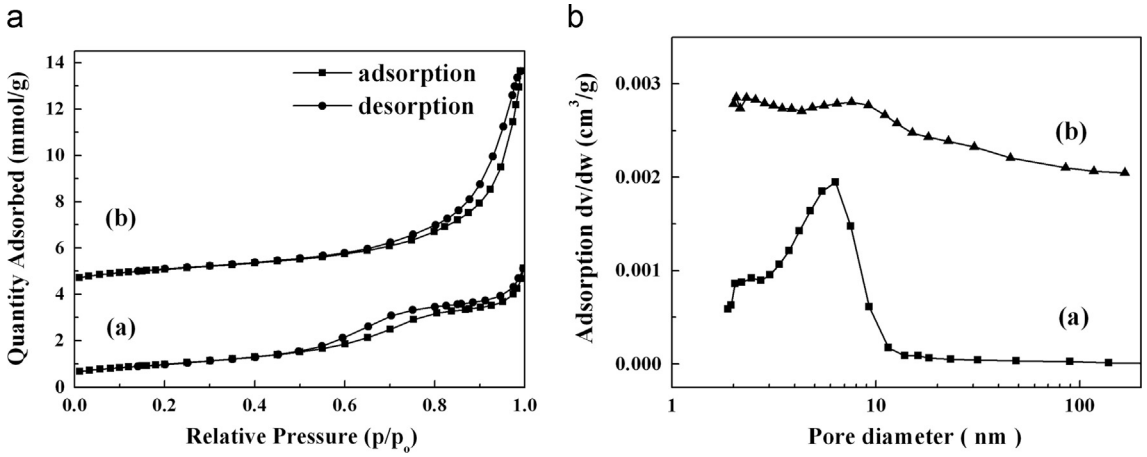

Fig. 3. N_2 adsorption/desorption isotherms (A) and the corresponding BJH pore size distributions (B) of the calcined materials: (a) Sample 1 and (b) Sample 2.

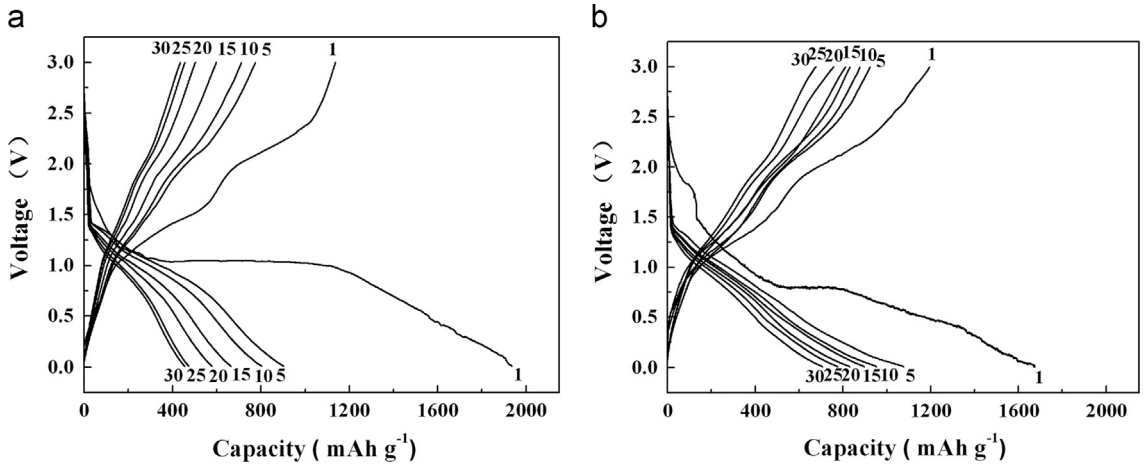

Fig. 4. Galvanostatic lithium-insertion/extraction curves of two electrodes at different cycling rates of 20, 40 and 60 mA g^{-1} between 0.01 and 3.0 V *vs.* Li/Li^+: (a) Sample 1 and (b) Sample 2.

Table 1
Charge/discharge specific capacities of two electrodes at various current densities.

Sample	Current density (mA g^{-1})	20	20	40	60
	Cycle number	1	10	20	30
Sample 1	Charge capacity (mAh g^{-1})	1137.3	712.3	503.5	435.8
	Discharge capacity (mAh g^{-1})	1935.7	803.9	578.8	455
Sample 2	Charge capacity (mAh g^{-1})	1195.2	877.9	812.5	676.8
	Discharge capacity (mAh g^{-1})	1674	953.2	830.8	706.1

current densities. The values of the Sample 2 electrode were maintained at 706.1 mAh g^{-1} after 30 cycles; it is much better than that of the Sample 1 electrode (455 mAh g^{-1}).

The relationships of charge and discharge capacity *vs.* cycle number for two electrodes at different current densities are given in Fig. 5. Two electrodes showed a fast capacity fading at the primal five cycles as shown in Fig. 5(a) and (b), especially Sample 1 showed the severe capacity fading. The capacity retention of Sample 2 is higher than that of Sample 1. After 20th cycles at the current density of 60 mA g^{-1}, the Sample 2 electrode was maintained above 800 mAh g^{-1}, which is close to the theoretical capacity of Co_3O_4 (890 mAh g^{-1}). Due to higher specific surface area of Sample 2, more spaces between the nanosheets are available. The nanostructure with MWCNTs enhanced the electrolyte/Co_3O_4 contact area, shortened the lithium ion diffusion length among the nanosheets, and accommodated the strain induced by the volume change during the electrochemical reaction.

Since the Sample 2 electrode had delivered better cycleability, it was chosen for further study in high power battery applications. As shown in Fig. 6, the Sample 2 electrode displayed a very high charge capacity of 1207 mAh g^{-1} at the current density of 50 mA g^{-1} (equivalent to 1 Li per formula unit in 2.6 h), which slightly reduced to 897.8, 804.1, 777.6, 710.9 and 672.5 mAh g^{-1} at the 10, 20, 30, 40 and 50th cycles, respectively. Although the cycling performance starts to show some fall off after 10 cycles, the capacity is still 1.8 times than the theoretical capacity of graphite (372 mAh g^{-1}) after more than 50 cycles. The nearly 100% capacity retention after 20 cycles is evidently believed to benefit from MWCNTs. Based on the results presented above, the Co_3O_4/MWCNTs

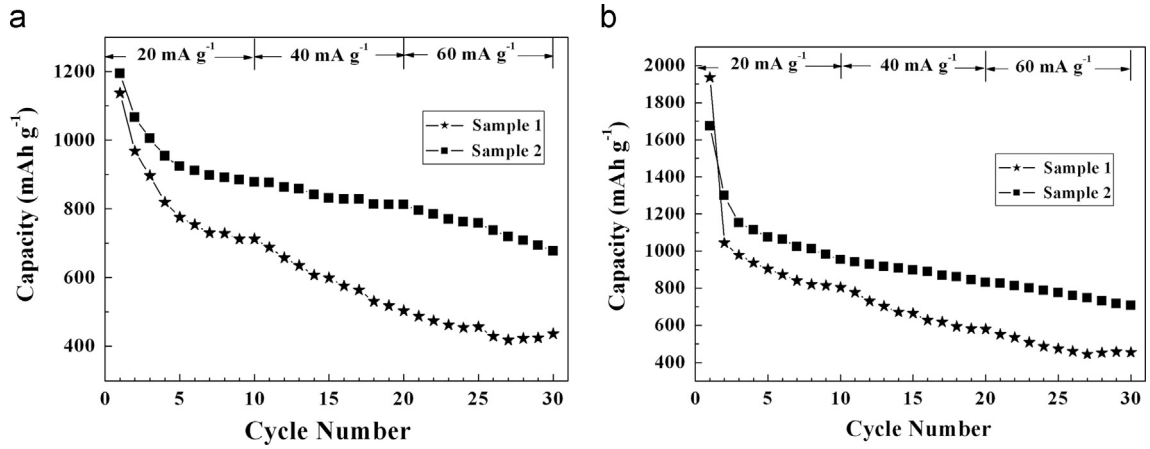

Fig. 5. consecutive cycling behaviors of two electrodes at various current densities between 0.01 and 3.0 V *vs.* Li/Li^+: (a) charge processes and (b) discharge processes.

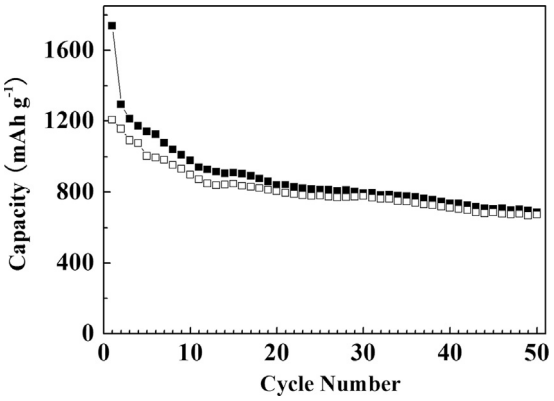

Fig. 6. Cycle life behavior of the Sample 2 electrode (the white and black squares represent charge and discharge processes, respectively) at a cycling rate of 50 mA g^{-1}.

composite shows better electrochemical performance than Co_3O_4 fabricated using the same technique. The most likely reasons are discussed as follows. Firstly, in the composite, the Co_3O_4 nanosheets are embedded among the carbon tube, which not only provides a flexible buffer to accommodate the volume change during lithium insertion/extraction, but also prevents the aggregation of the cobalt oxide nanoparticles and stabilizes the cycling performance of the composite material [21]. Thus, the composite electrode exhibits excellent cycling performance. Secondly, the lithium ion diffusion significantly depends on the transport length and specific surface area of the material [22]. In the present case, the nanoscale materials decrease the ion diffusion length, which results in a large electrode/electrolyte contact area and a short average path length for lithium ion transport. Thus, the nanosheets exhibit high rate capability and good coulombic efficiency [23]. Thirdly, the MWCNTs have high electrical conductivity, which decreases the interior resistance of the electrodes and is good for balancing the electronic and ionic conductivity [24]. Therefore, the Co_3O_4/MWCNTs composite nanosheets are considered to be good candidates as anode material for LIBs.

EIS is a powerful tool to identify the kinetics of lithium intercalation/deintercalation into the electrodes. The measured impedance of the electrochemical cell is a collective response of kinetic processes occurring on the electrode. In the present study, the possible and experimentally visualized processes are a resistive component arising from the electrolyte resistance and cell components, the double-layer capacitance of the surface film and the associated impedance, the impedance associated with the bulk of the active material and the capacitance associated with it, the charge transfer (electron transfer) resistance of the intercalation reaction and the capacitance, and a Warburg contribution which is characteristic of the lithium ion diffusion through the bulk of the active material [25–28]. Fig. 7 presents the Nyquist impedance plots of two electrodes. The electrochemical impedance spectroscopy (EIS) tests at the fresh and 10, 20, 30th recharged states were carried out to investigate the relationship of the AC impedance spectra and the cycling behaviors. All spectra consist of a depressed semicircle in the high-to-medium frequency range and a straight line in the low frequency range. The semicircles in the high-to-medium frequency regions correspond to the charge-transfer impedance of the electrode/electrolyte interface. The variations observed in the semicircle are attributed to the structural changes in the reactive surface of the electrode due to the dissolution of lithium and the oxidation of cobalt [29]. The inclined line at an approximate 45° angle to the real axis corresponds to the lithium-diffusion processes within the electrode [30]. The semicircles in the medium-frequency region in Fig. 7(a) showed a rapid increase, which were different with the semicircles in Fig. 7(b). It indicated that the impedances of Sample 1 increased with the charge–discharge progress because of the collapse of the structure and the aggregation of nanoparticles. The charge-transfer impedances of Sample 1 are bigger than those of Sample 2. Considering the charge–discharge results, it is believed that MWCNTs have a high electrical conductivity, resulting in a decrease of the interior resistance of the electrodes. From the EIS tests, it is clear that the charge transfer resistance variations of Sample 2 are less than those of

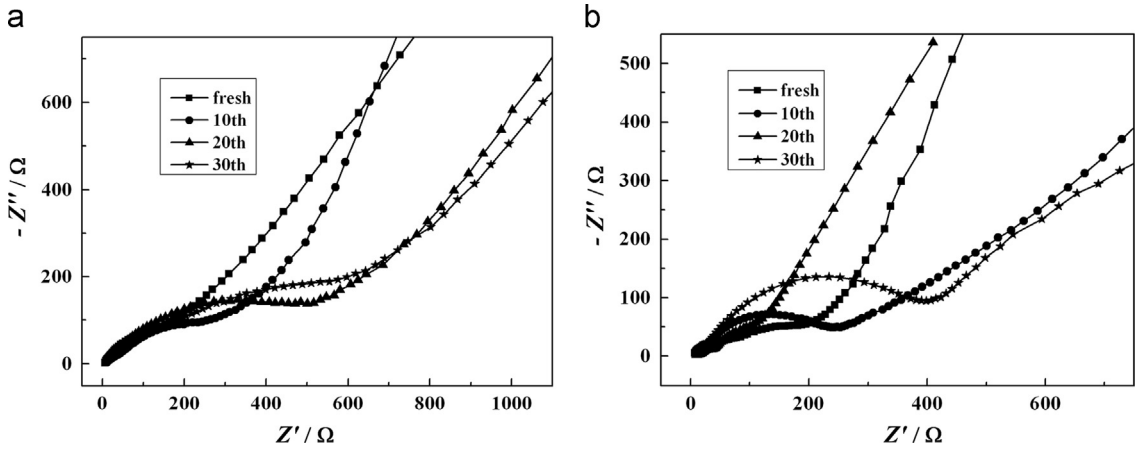

Fig. 7. AC impedance spectra of the calcined materials: (a) Sample 1 and (b) Sample 2 measured at the open potential at fresh and 10, 20, and 30th recharged states.

Sample 1 and the lithium ion charge-transfer impedance of the Sample 2 electrode is smaller than that of Sample 1, which indicate that the Sample 2 electrode has fewer structural changes and the smaller lithium ion charge-transfer impedance during cycling. This is in good agreement with the improved electrochemical performance of the Sample 2 electrode.

4. Conclusions

In summary, Co_3O_4/MWCNTs composites have been synthesized by a simple hydrothermal method by using a surfactant (CTAB) and a precipitation agent (urea). The Co_3O_4/MWCNTs electrode displayed an improved cycleability and maintained 706.1 mAh g^{-1} after 30 cycles; it is much better than that of the Co_3O_4 electrode (455 mAh g^{-1}). At a current density of 50 mA g^{-1}, 897.8, 804.1, 777.6, 710.9 and 672.5 mAh g^{-1} reversible capacities at the 10, 20, 30, 40 and 50th cycles were obtained, respectively. The nearly 100% capacity retention after 20 cycles is evidently believed to benefit from MWCNTs. The improvement of electrochemical performance is attributed to the effects of MWCNTs that possess properties including their excellent electric conductivity and large surface area, which is beneficial for alleviating the effect of volume variation, shortening the distance of lithium ion diffusion, facilitating the transmission of electrons and keeping the structure stable. EIS tests further indicated that the Co_3O_4/MWCNTs electrode had less structural changes during cycling, which is in agreement with better electrochemical performances.

Acknowledgments

This work was financially supported by the National Natural Science Foundation of China (No. 21203120) and the Shanghai Government (Nos. 11ZR1435900, 10ZR1415400, YJ2011-11, 10JC1406900, and 12YZ163).

References

[1] B. Koo, H. Xiong, M.D. Slater, V.B. Prakapenka, M. Balasubramanian, P. Podsiadlo, C.S. Johnson, T. Rajh, E.V. Shevchenko, Nano Lett. 12 (2012) 2429–2435.
[2] J.H. Lee, Y.H. Kwon, B.H. Kong, J.Y. Lee, H.K. Cho, Cryst. Growth Des. 12 (2012) 2495–2500.
[3] T. Zhu, J.S. Chen, X.W. Lou, J. Phys. Chem. C 116 (2012) 6873–6878.
[4] L. Tian, H.L. Zou, J.X. Fu, X.F. Yang, Y. Wang, H.L. Guo, X.H. Fu, C. L. Liang, M.M. Wu, P.K. Shen, Q.M. Gao, Adv. Funct. Mater. 20 (2010) 617–623.
[5] Y. Liu, C. Mi, L. Su, X. Zhang, Electrochim. Acta 53 (2008) 2507–2513.
[6] X. Wang, A. Sumboja, E. Khoo, C. Yan, P.S. Lee, J. Phys. Chem. C 116 (2012) 4930–4935.
[7] Y. Liu, X. Zhang, Y. Wu, Mater. Chem. Phys. 128 (2011) 475–482.
[8] W.M. Zhang, X.L. Wu, J.S. Hu, Y.G. Guo, L.J. Wan, Adv. Funct. Mater. 18 (2008) 3941–3946.
[9] H. Qiao, L.F. Xiao, Z. Zheng, H.W. Liu, F.L. Jia, L.Z. Zhang, J. Power Sources 185 (2008) 486–491.
[10] Y. Sharma, G.V.S. Rao, B.V.R. Chowdari, Adv. Funct. Mater. 17 (2007) 2855–2861.
[11] N. Jayaprakash, W.D. Jones, S.S. Moganty, L.A. Archer, J. Power Sources 200 (2012) 53–58.
[12] L. Zhan, Y. Wang, W. Qiao, L. Ling, S. Yang, Electrochim. Acta 78 (2012) 440–445.
[13] J.R. Dahn, T. Zheng, Y. Liu, J.S. Xue, Science 270 (1995) 590–595.
[14] W.J. Kim, E.Y. Jang, D.K. Seo, T.J. Kang, K.C. Jin, D.H. Jeong, Y.H. Kim, Langmuir 26 (20) (2010) 15701–15705.
[15] A.L.M. Reddy, S. Ramaprabhu, J. Phys. Chem. C 111 (21) (2007) 7727–7734.
[16] S. Liao, K.A. Holmes, H. Tsaprailis, V.I. Birss, J. Am. Chem. Soc. 128 (11) (2006) 3504–3505.
[17] M.M. Shaijumon, S. Ramaprabhu, N. Rajalakshmi, Appl. Phys. Lett. 88 (2006) 253105–253108.
[18] J. Chen, Y. Liu, A.I. Minett, C. Lynam, J. Wang, G.G. Wallace, Chem. Mater. 19 (2007) 3595–3597.
[19] L.J. Fu, H. Liu, H.P. Zhang, C. Li, T. Zhang, Y.P. Wu, R. Holze, H.Q. Wu, Electrochem. Commun. 8 (2006) 1–4.
[20] T. Zhang, J. Gao, H.P. Zhang, L.C. Yang, Y.P. Wu, H.Q. Wu, Electrochem. Commun. 9 (2007) 886–890.
[21] S.M. Paek, E. Yoo, I. Honma, Nano Lett. 9 (2009) 72–75.
[22] B. Varghese, T.C. Hoong, Z. Yanwu, M.V. Reddy, B.V.R. Chowdari, A. T.S. Wee, T.B.C. Vincent, C.T. Lim, C.H. Sow, Adv. Funct. Mater. 17 (2007) 1932–1939.
[23] P. Zhang, Z.P. Guo, Y. Huang, D. Jia, H.K. Liu, J. Power Sources 196 (2011) 6987–6991.

[24] Z.S. Wu, W. Ren, L. Wen, L. Gao, J. Zhao, Z. Chen, G. Zhou, F. Li, H. M. Cheng, ACS Nano 4 (2010) 3187–3194.
[25] Y. Liu, X. Zhang, Solid State Ion. 231 (2013) 63–68.
[26] F. Nobili, F. Croce, B. Scrosati, R. Marassi, Chem. Mater. 13 (2001) 1642–1646.
[27] W. Lai, F. Ciucci, J. Electrochem. Soc. 158 (2) (2011) A115–A121.
[28] K.M. Shaju, G.V.S. Rao, B.V.R. Chowdari, J. Electrochem. Soc. 150 (1) (2003) A1–A13.
[29] M.J. Escudero, T. Rodrigo, J. Soler, L. Daza, J. Power Sources 118 (2003) 23–34.
[30] S. Yang, H. Song, X. Chen, Electrochem. Commun. 8 (2006) 137–142.